

GT2011-4), \$(

TOWARDS LARGE-EDDY SIMULATION OF TURBULENT FLOW IN A CENTRIFUGAL IMPELLER

Gorazd Medic

United Technologies Research Center
411 Silver Lane, East Hartford, CT 06108, USA

Jinzhang Feng

United Technologies Research Center
411 Silver Lane, East Hartford, CT 06108, USA

Liwei Chen

United Technologies Research Center (China) Ltd.
Room 3512, 35/F, Shanghai World Financial Center, 100
Century Avenue, Pudong, Shanghai, 200120, P.R.China

Om Sharma

United Technologies Research Center
411 Silver Lane, East Hartford, CT 06108, USA

ABSTRACT

Large-eddy simulation (LES) using wall-adapting local eddy-viscosity (WALE) subgrid scale model has been applied towards elucidating the complex turbulent flow physics in a centrifugal impeller. Several canonical cases of increased complexity were analyzed to better understand the advantages and challenges of applying the LES framework to the aforementioned target problem. These include turbulent flow in a rotating channel, a straight and a curved duct. Results obtained with LES are compared in detail with two-equation eddy-viscosity Reynolds Averaged Navier-Stokes (RANS) turbulence models widely used in industry, as well as, for some of the canonical cases, with hybrid RANS/LES approaches such as the detached eddy simulation (DES) and scale-adaptive simulation (SAS). Finally, LES has been applied to turbulent flow in NASA CC3 centrifugal impeller with grids of increased resolution (up to 100 million computational cells per passage).

NOMENCLATURE

u_τ	friction velocity
U_b	bulk velocity
Re_τ	friction velocity based Reynolds number
Re_b	bulk velocity based Reynolds number
u^+	streamwise velocity in inner coordinates
y^+	wall distance in inner coordinates
u_{rms}	root-mean-square of streamwise velocity
h	channel half-height (for periodic channel cases)

D	hydraulic diameter
x_c	x-coordinate of the center of the bend (for curved duct)
y_c	y-coordinate of the center of the bend
z_c	z-coordinate of the center of the bend
R_c	radius of curvature for the bend
$(r - r_o)/(r_i - r_o)$	non-dimensional coordinate for the bend
De	Dean number
TKE	turbulent kinetic energy
SST	shear stress transport model
S/S	suction side
P/S	pressure side

INTRODUCTION

Background

Flow in a centrifugal impeller contains several features that have over the years proven to be very challenging for RANS turbulence models. These include strong rotational effects due to the high rotational speeds necessary to achieve high pressure ratio; strong curvature of the hub and shroud surfaces (with the flowpath changing from axial inflow to radial outflow); large tip-clearance vortices that typically migrate downwards and occupy a large portion of the flow passage; and finally, at the impeller exit, the presence of flows with low streamwise velocity near the shroud including separation.

Two-equation linear eddy-viscosity RANS turbulence models typically struggle to correctly predict these flow

features. More advanced RANS turbulence models designed to capture these effects have also been introduced over the years (see [1-2]), but seemed to have gained little traction due to issues with numerical stiffness, and inconsistent results.

In order to really elucidate turbulent flow physics in such configurations, higher fidelity modeling is required. In this analysis, large-eddy simulation using the WALE subgrid-scale model introduced in [3] is employed to analyze the flow in a centrifugal impeller. Analyses on three simple canonical flows, namely, a spanwise rotating channel [14], a straight square duct [15] and a square duct with a 90 degree turn [16-17], are conducted to investigate the aforementioned critical features of flows in centrifugal impellers. Detailed comparisons are made to the available data to assess the ability of LES to predict these flows; comparisons to standard RANS turbulence models typically employed in turbomachinery CFD analyses are also included. Finally, LES of the flow in the NASA CC3 centrifugal impeller [20] is conducted on several computational grids.

COMPUTATIONAL FRAMEWORK

Large-eddy simulation

In the LES framework, Navier-Stokes equations for the filtered velocity \bar{u}_i are solved in the entire computational domain, and unresolved turbulence scales are modeled with a subgrid scale model. Here, the WALE model [3] is employed for the subgrid scale viscosity:

$$\nu_t^{SGS} = (C_w \Delta)^2 \frac{(S_{ij}^d S_{ij}^d)^{3/2}}{(\bar{S}_{ij} \bar{S}_{ij})^{5/2} + (S_{ij}^d S_{ij}^d)^{5/4}},$$

where \bar{S}_{ij} is the strain rate tensor for the resolved field. S_{ij}^d is defined as

$$S_{ij}^d = \frac{1}{2}(\bar{g}_{ij}^2 + \bar{g}_{ji}^2) - \frac{1}{3} \delta_{ij} \bar{g}_{kk}^2,$$

with $\bar{g}_{ij}^2 = \frac{\partial \bar{u}_i}{\partial x_k} \frac{\partial \bar{u}_k}{\partial x_j}$ and δ_{ij} the Kronecker symbol. The model

constant $C_w = 0.5$ was calibrated numerically for decaying isotropic turbulence.

For some of the cases, notably the rotating channel, hybrid RANS/LES techniques based on the k-omega RANS turbulence model [7], such as DES [4-5] and SAS [6], were also used, with the goal of assessing these hybrid approaches in the presence of rotation. The SST-based DES proposed by Strelets [4], in which the dissipation term in the k-equation can be rewritten as

$$D_{RANS}^k = \rho \beta' k \omega = \rho k^{3/2} / l_{k-\omega}$$

where $l_{k-\omega} = k^{1/2} / (\beta' \omega)$ represents a turbulence length scale.

By introducing $\tilde{l} = \min(l_{k-\omega}, C_{DES} \Delta)$ with $\Delta = \max(\Delta_i)$, the dissipation term becomes $D_{DES}^k = \rho k^{3/2} / \tilde{l}$.

The SST-based SAS can be derived by adding the term

$$Q_{SAS} = \rho \max \left\{ 2.65 \frac{L}{L_{vk}} |S|^2 - 6k \max \left[\frac{|\nabla \omega|^2}{\omega^2}, \frac{|\nabla k|^2}{k^2} \right], 0 \right\} \text{ to the}$$

ω -equation, where $L = \sqrt{k} / (C_\mu^{1/4} \omega)$, the L_{vk} is von Karman

$$\text{length } L_{vk} = \max \left[\frac{\kappa |S|}{|\nabla^2 U|}, \frac{0.358 C_\mu \Delta}{\beta - C_\mu \alpha} \right] \text{ and } |S|^2 = 2S_{ij} S_{ij}.$$

Numerical considerations

Flow solver used in these simulations is based on a second-order accurate numerical method (both in space and time) for compressible flow equations first presented in [8]. Traditionally, when this method has been applied within the RANS framework for transonic flows in turbomachinery in the past, artificial viscous damping was always added. In the cases presented in this work, including the centrifugal impeller, no artificial damping was included. However, when applied to LES of flows with shocks, artificial damping is again required in the vicinity of discontinuities and a careful hybridization of this damping operator with the second-order scheme is warranted. Fine-tuning of damping trigger and magnitude in the context of LES is a subject of an extensive ongoing research in the community.

Commercial CFD solver CFX [9] was also used for some of the smaller benchmark runs presented in this paper (rotating channel, straight and curved duct). Second-order spatial discretization (CD) was then used for convective terms in those computations.

Decay of homogeneous isotropic turbulence

The decay of homogeneous isotropic turbulence experiment [10] is a standard test of the adequacy of numerical discretization and subgrid scale models in LES solvers for capturing the complex interactions of decaying turbulent vortex structures.

The experimental setup is modeled by considering a freely decaying turbulent fluid in a box with periodic boundary conditions. The method proposed in [11] is used to generate the initial velocity field in the spectral space (based on Von Karman spectrum), which is then converted to physical space using inverse FFT. Energy spectra computed with a second-order discretization and WALE subgrid scale model (with $C_w = 0.5$) on three different grids (32^3 , 64^3 and 128^3) are compared to measurements in Fig. 1. LES computed on the first two grids show good agreement with data at high wave numbers, thus validating both the chosen subgrid scale model and the numerical discretization. As the grid is further refined, the role of the subgrid scale model is reduced. The results on the finest grid converge even closer to the data further validating the numerical approach.

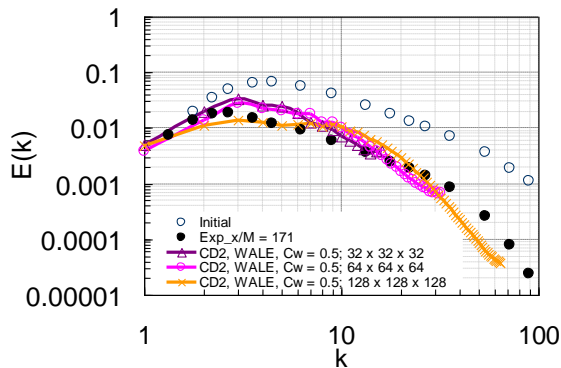


Fig. 1 Decay of homogeneous isotropic turbulence computed using WALE subgrid-scale model on different grids. Energy spectra at non-dimensional time $t U_0/M = 171$.

Periodic channel flow

Turbulent flow in a periodic channel at friction velocity u_τ based Reynolds number $Re_\tau = u_\tau h/\nu$ of 395 is another standard test for LES solvers [12]. It is used to assess the numerical dissipation and its impact on capturing small turbulent structures in the boundary layer (for illustration, streamwise vortices in the vicinity of solid walls are presented in Fig 2).

In this study, the setup is fairly standard. The grid consists of $80 \times 64 \times 64$ computational cells and the computational domain has the dimensions of $2\pi h \times 2h \times \pi h$ in the streamwise, wall-normal and spanwise directions. No-slip boundary condition is used on the channel walls and periodic boundary conditions are employed in the streamwise and spanwise directions. The time step size is $0.0001 h/u_\tau$.

A comparison of mean and rms velocities to DNS data is presented in Fig 3a. Typically, at this resolution the rms velocities, the u_{rms} velocity in particular, is overpredicted. By further refining the grid (to a resolution of $160 \times 128 \times 128$ computational cells) the rms velocities converge closer to DNS data (Fig. 3b).

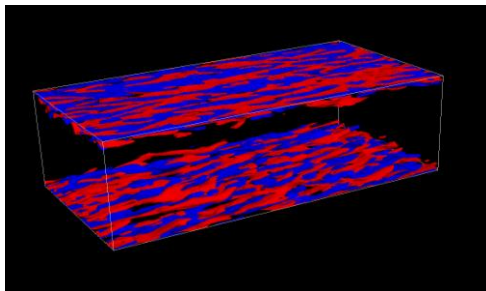


Fig. 2 Periodic channel flow at $Re_\tau = 395$ computed using WALE subgrid-scale model on a $80 \times 64 \times 64$ grid. Isosurfaces of instantaneous streamwise vorticity.

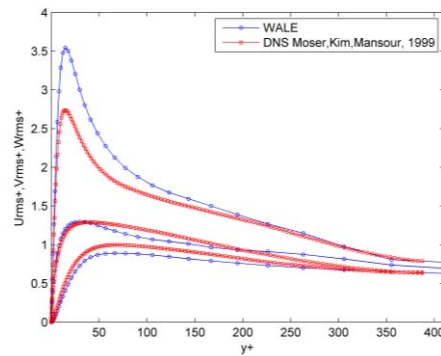
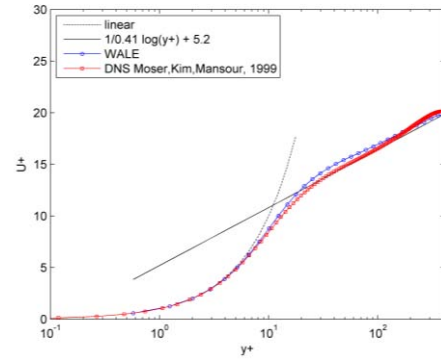


Fig. 3a Periodic channel flow at $Re_\tau = 395$ computed using WALE subgrid-scale model on a $80 \times 64 \times 64$ grid. Mean and rms velocities – comparison to DNS [12].

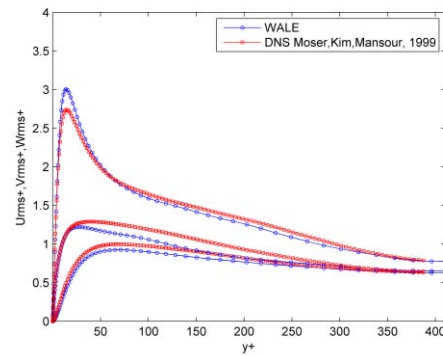


Fig. 3b Periodic channel flow at $Re_\tau = 395$ computed using WALE subgrid-scale model on a $160 \times 128 \times 128$ grid. Rms velocities – comparison to DNS [12].

CANONICAL TEST CASES

Rotating channel

This case is defined by the following parameters: the Reynolds number and the rotation number, which are defined as $Re_\tau = u_\tau h/\nu$ and $N_\tau = 2\Omega h/u_\tau$, with Ω being the rotation speed, ν the kinematic viscosity, h the half-height of the channel and u_τ the friction velocity. As above, the no-slip boundary condition is used on the channel walls and periodic boundary conditions are employed in the streamwise and

spanwise directions. In the present study, the Reynolds number Re_τ is chosen as 194 to match the DNS simulations [13-14] and the rotation number N_τ varies from 0 to 7.5.

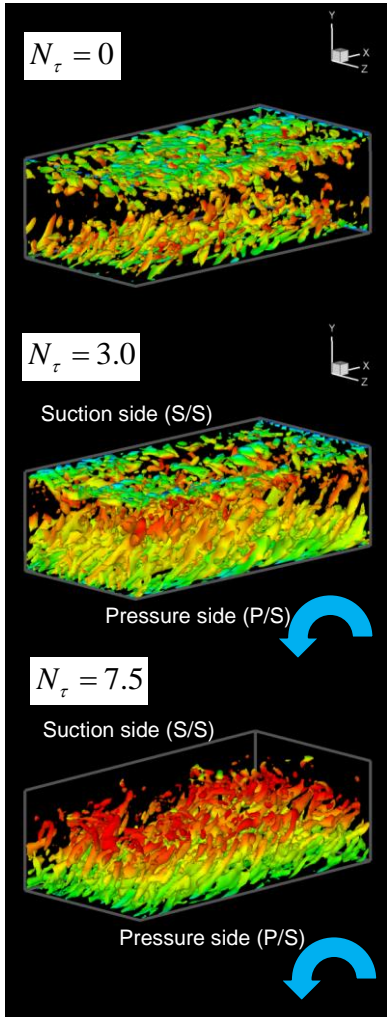


Fig. 4 Rotating channel flow at $Re_\tau = 194$ for various N_τ computed using WALE subgrid-scale model on a $32 \times 48 \times 32$ grid. Isosurfaces of instantaneous $Q = |\Omega|^2 - |S|^2$.

Two computational grids were used for LES, a coarser one consisting of $32 \times 48 \times 32$ computational cells, and the finer one with $100 \times 64 \times 64$ computational cells. DES and SAS were also assessed for this case and for those approaches only the coarser grid was used. Computational domain has the same size as for the previous test case, $2\pi h \times 2h \times \pi h$ in streamwise, wall-normal and spanwise directions. The time step size is approximately $0.001 h/u_\tau$.

As shown in Fig. 4, as the channel is submitted to rotation the boundary layers along the two solid walls start to change. On the pressure side, the turbulence is enhanced and on the suction side, turbulence is suppressed. This is illustrated by plotting the vertical structures visualized by isosurfaces of

instantaneous $Q = |\Omega|^2 - |S|^2$, and colored by the velocity magnitude.

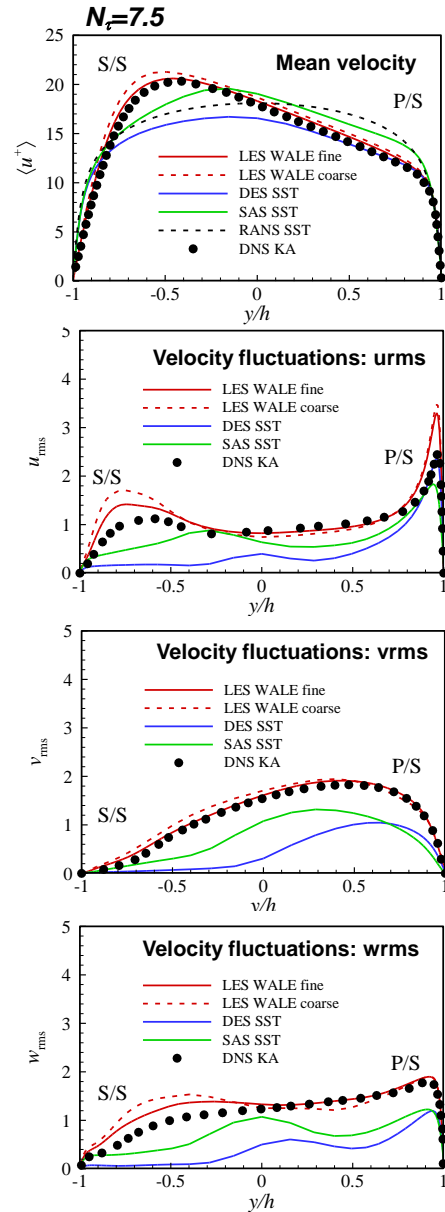


Fig. 5 Rotating channel flow at $Re_\tau = 194$ for $N_\tau = 7.5$, computed using WALE subgrid-scale model on a $32 \times 48 \times 32$ and $100 \times 64 \times 64$ grid, as well as results from $k-\omega$ based DES and SAS. Comparison of mean and rms velocities with DNS [14].

Time-averaged results are further compared to the aforementioned DNS. In particular, for $N_\tau = 7.5$, the mean velocities obtained using different approaches are shown in Fig. 5. Two equation linear eddy-viscosity RANS models (here SST $k-\omega$ was used) typically cannot capture the asymmetric profiles of the mean velocity. LES results, on the other hand, compare favorably with the DNS data, with the results improving as the grid is refined. DES provides a good

prediction on the pressure side, but fails on the suction side. For SAS, the mean velocity profile is over-predicted.

As shown in the bottom of Fig. 5, rms velocities predicted by LES are consistent with the DNS data (again improving as the grid is refined), while rms velocities predicted by SAS and DES are much lower than DNS data, especially on the suction side.

Straight duct

Large-eddy simulation of turbulent flow in a straight square duct is conducted next. This case can then be used to generate turbulent inflow fluctuations for the curved duct case considered in the next section.

The size of the computational domain is $12.8D \times D \times D$, in the streamwise and transverse directions, where D is the hydraulic diameter, chosen as 0.04m (see Fig 6.). To validate the present simulation, we compare LES results for mean streamwise and secondary velocities, as well as rms velocities to DNS data [15] (for $Re_\tau = 300$, or bulk-velocity based Reynolds number of $Re_b = 4410$). The periodic boundary conditions are employed in the streamwise direction with the mass flow rate kept constant.

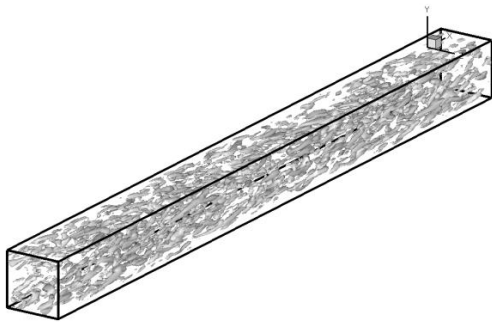


Fig. 6 Square duct at $Re_\tau = 300$ - turbulent structures (visualized as isosurfaces of instantaneous Q).

The computational grid of $120 \times 60 \times 60$ computational cells and the time-step of approximately $0.001D/U_b$ was chosen for this simulation (where U_b is the bulk velocity). Turbulence statistics were obtained after flow has evolved for more than $T = 10D/U_b$ (to increase the statistical sampling, symmetries are utilized).

Fig. 7 presents a comparison of the mean streamwise velocity from an LES with the one computed with the SST k-omega model. As expected, the two-equation, linear eddy-viscosity RANS turbulence models cannot capture the secondary flow features, whereas LES is more successful at that.

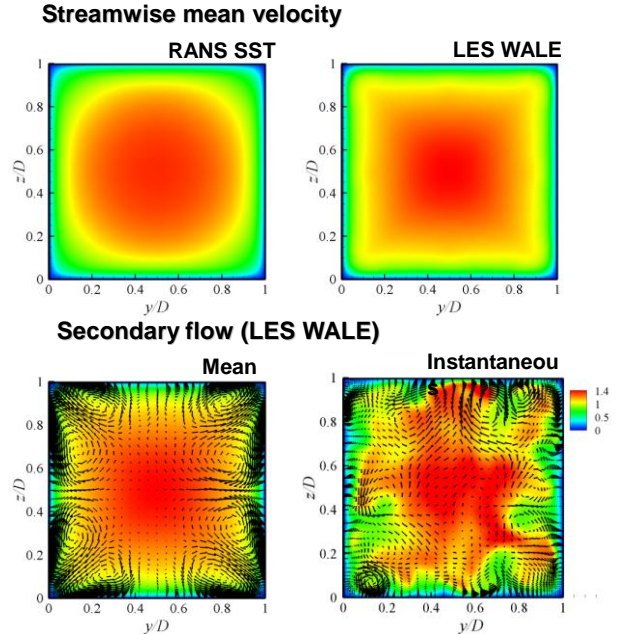


Fig. 7 Square duct at $Re_\tau = 300$. Contours of mean and instantaneous streamwise velocity.

Fig. 8 presents the profiles of the normalized streamwise and transverse mean velocity U/U_b and W/U_b at different z cross-sections (different “spanwise” locations in the duct) and are compared with the DNS data. The transverse velocity profiles from LES clearly demonstrate the presence of the secondary flows. As a result, the streamwise velocity profiles are also better predicted by LES than by RANS.

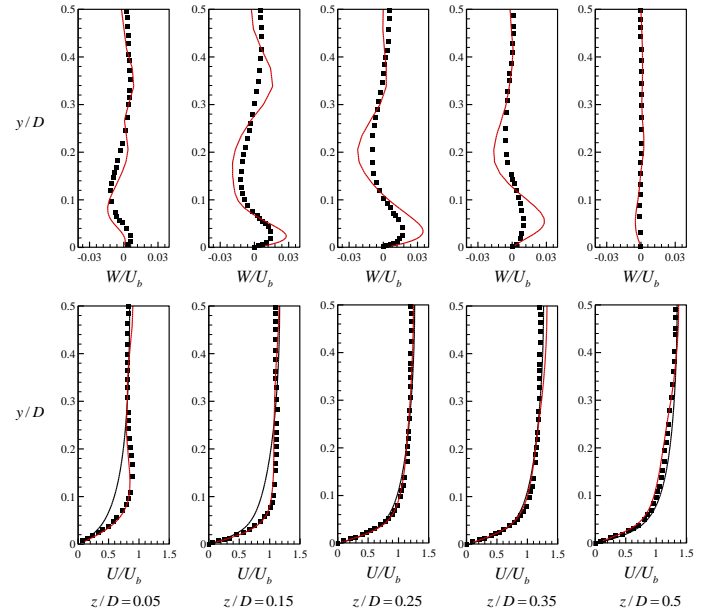


Fig. 8 Square duct at $Re_\tau = 300$. Streamwise (bottom) and transverse (top) velocity profiles. RANS SST result is presented in black, LES WALE in red and DNS data with symbols.

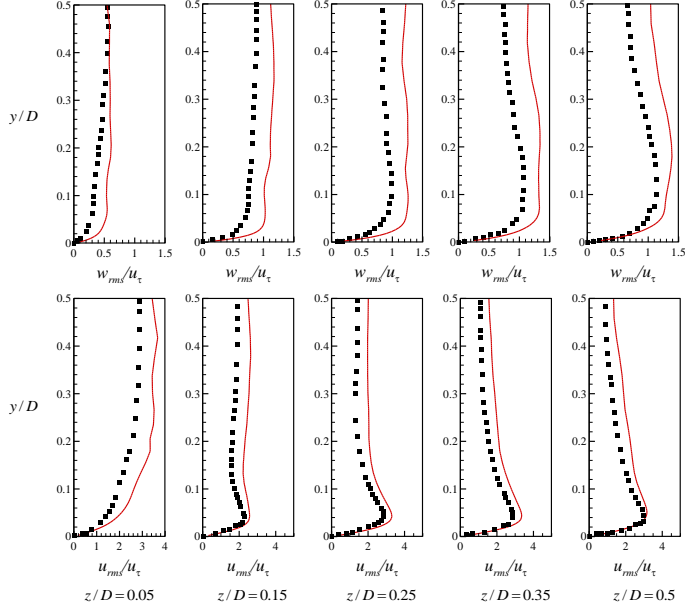


Fig. 9 Square duct at $Re_\tau = 300$. Streamwise (bottom) and transverse (top) rms velocities. LES (red) and DNS (symbols).

Streamwise and transverse rms velocities from the LES computations are further compared to DNS data for various z cross-sections in Fig. 9. LES predicts somewhat higher rms velocities than DNS due to relatively coarse grid used in the present study.

Curved duct

LES and RANS studies of the turbulent flow in a curved duct are carried out. Following the experimental setup from [16-17], the configuration used in the present study is a 90 degree square bend of mean radius $R_c = 2.3D$ (0.092m). The inlet boundary is at $x = -2.5D$ (-0.1m), the outlet boundary at $y - y_c = 6D$, and the exit from the bend at $y = y_c$. D is the hydraulic diameter (0.04m) and y_c is the y-coordinate of the center of bend (see Fig. 10). The computational grid consists of $160 \times 80 \times 80$ cells in the streamwise and transverse directions. No-slip boundary conditions are applied on all walls. Finally, Dean number $De = Re_b \sqrt{D/(2R_c)}$ characterizing the flow equals 2056.

The Reynolds number at consideration here in this initial analysis is the same as the one used for the straight duct ($Re_b = 4410$), which is significantly lower than the one used in the experiments ($Re_b = 40,000$). The focus will thus be on comparing LES to RANS and assessing the differences between the two approaches.

To provide a fully developed turbulent inlet boundary condition for the bend duct, the mean velocity profile from the straight duct ($Re_b = 4410$) is imposed at the inlet, and at the same time, time-dependent disturbances are introduced to represent turbulent fluctuations following the simple approach

of [18]. Turbulent fluctuations from the square duct simulation could also be used following the recycling/rescaling technique presented in [19].

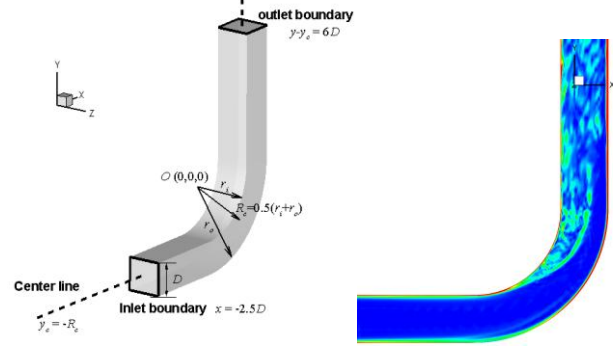


Fig. 10 Curved duct. Domain layout and contours of instantaneous streamwise vorticity at mid-duct z -plane.

The distributions of mean streamwise velocity computed by RANS and LES at different streamwise cross-sections are shown in Fig. 11. At 45° plane, the mean streamwise velocity by both RANS and LES exhibits an acceleration of the fluid moving near the inner wall ($(r - r_o)/(r_i - r_o) = 1.0$) due to curvature effects, as shown in the left of Fig. 11. Near the outer wall ($(r - r_o)/(r_i - r_o) = 0$), the result obtained by LES displays a thicker boundary layer resulting from same curvature effects mentioned above. At the plane $y - y_c = 2.5D$ downstream of the bend, as shown on the right of Fig. 11, the secondary flow motion is less severe in LES than in RANS.

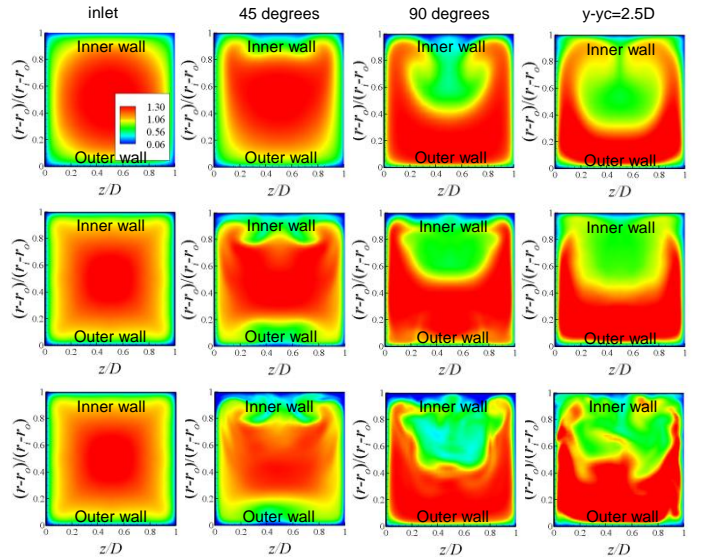


Fig. 11 Curved duct. Streamwise velocity at different locations in the duct, RANS SST (top), LES WALE averaged (middle) and instantaneous (bottom).

To characterize turbulent fluctuations in the curved duct, the contours of the TKE, $\langle k \rangle = 0.5 \langle u_i' u_i' \rangle / U_b^2$, are shown in Fig. 12 at various streamwise cross-sections. Downstream of the bend TKE has large values in the center of the duct due to the strong secondary flow, but the values predicted by RANS are smaller than those predicted by LES. In addition, note that in the LES there are large values of TKE in the corners at the outer wall; this is associated with the small secondary vortices predicted by LES. This kind of phenomenon is not captured by RANS.

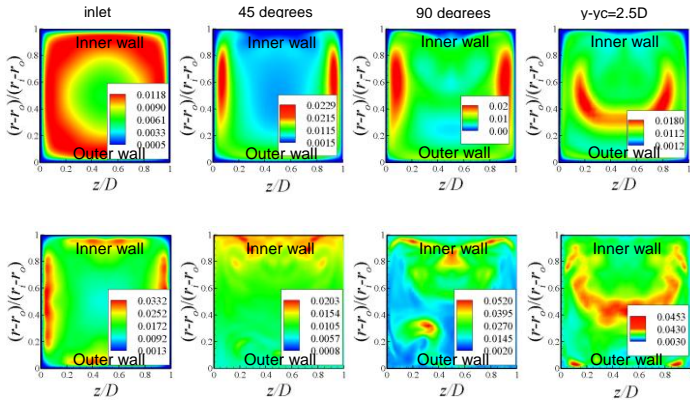


Fig. 12 Curved duct. Turbulent kinetic energy at different locations in the duct, RANS SST (top), LES WALE averaged (bottom).

CENTRIFUGAL IMPELLER

Turbulent flow in NASA CC3 centrifugal impeller with vaneless diffuser (described in detail in [20]) is considered next. These initial computations are performed at design operating point (with the flow rate of approx 10 lb/s).

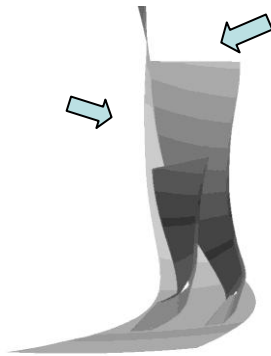


Fig. 13 NASA CC3 impeller passage layout [11]; it includes the main and splitter blades.

The single passage consists of a main blade and a splitter blade. The grid topology used for the grid surrounding each is the HHHHO topology (+ tip clearance blocks), resulting in 12 blocks. The initial RANS-quality grid has about 1.2 million computational cells. The subsequent LES grids were obtained

by progressively refining the initial grid in all three directions, first to a grid of approximately 9 million cells, and then to an even finer grid of about 81 million cells (see Fig. 14).

Time-step size was initially chosen as approximately $0.001 T_{FT}$, and the simulations were computed for about $15 T_{FT}$. One flow-through time is defined here as $T_{FT} = L_{passage}/U_b$. Computations were performed on 40 Xeon X5550 2.66 GHz CPUs for about 250 hours. This time step corresponds to Δt^+ of about 10, which is somewhat large (typically Δt^+ closer to 1 is required). Thus, a sensitivity study for the required time-resolution is also being pursued.

As a part of getting all the tools ready, the LES solver was initially tested on the coarser grid. This grid is obviously inappropriate for the Reynolds number of the flow in this case (the Reynolds number is in the lower hundred thousands, depending on the dimensions chosen for its definition, e.g. inlet passage hydraulic diameter, outlet passage hydraulic diameter). Focus then switched to the finer grid, and all the results presented below are from the finer grid (81 million cells) simulation.

Performance predictions with this fine grid indicate that the losses are still underpredicted compared to the initial RANS simulation, and the data. The measured adiabatic efficiency was 86.77, RANS predicts 88.97, and this finer grid LES predicts an average value of about 91.35. The current LES analysis over-predicted the adiabatic efficiency for about 2.5 points, when compared to RANS. Similarly, the measured total pressure ratio was 4.174, RANS predicted 4.357, and the finer grid LES 4.373.

It is likely that even this 80 million grid is still not sufficiently fine to resolve the near-wall region and further grid refinement and corresponding LES analyses are on-going. In order to better assess the current resolution, the near-wall grid on the suction side of the main blade at mid-chord (and mid-span) has been examined; it has $\Delta x^+ \sim 50$, $\Delta z^+ \sim 20$, with Δy^+ well below 1 (with x,y and z the local streamwise, wall-normal and spanwise directions). To be able to resolve the near-wall turbulent structures, resolution closer to $\Delta x^+ \sim 30$, $\Delta z^+ \sim 10$ is preferred, indicating that further refinement might be necessary.

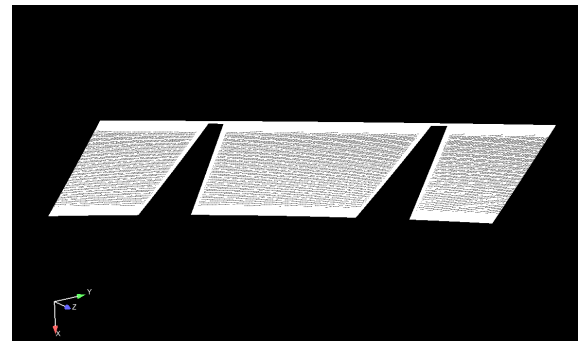


Fig. 14a NASA CC3 computational grid; cross-section at a constant radius near the trailing edge.

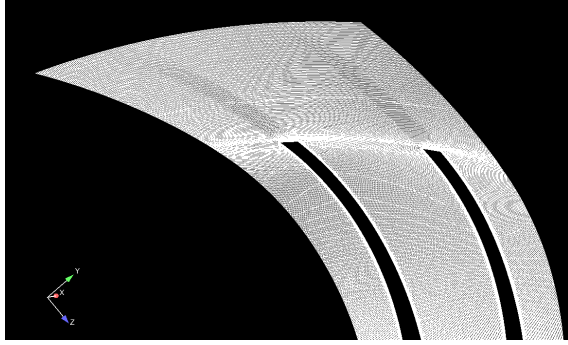


Fig. 14b NASA CC3 computational grid; constant axial cross-section near the shroud.

Figs. 15-17 present turbulent structures (again, visualized using Q) on the suction side leading edge of the main blade, on the suction side of the leading edge of the splitter blade and on the pressure side of the leading edge of the main blade, respectively. Surprisingly, very elongated coherent structures are present in the vicinity of the leading edge on the suction side of both blades. Obviously, these features depend strongly on inlet boundary conditions (turbulence free in this case) and grid resolution (most likely, still insufficient). On the pressure side, at the leading edge no such structures are present and there is a seemingly laminar region in the vicinity of the hub. This will strongly depend on the state of the boundary layer on the hub as it approaches the leading edge, and that in turn depends on the inlet boundary conditions, so a sensitivity study is warranted.

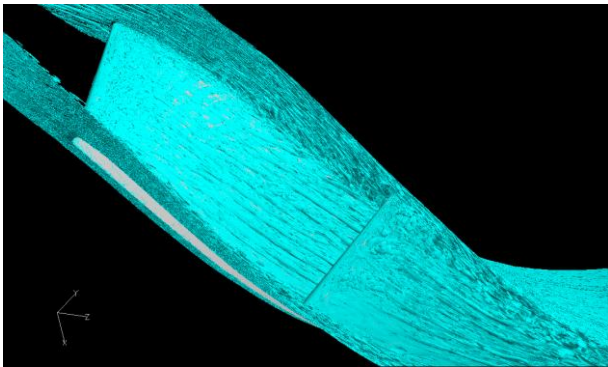


Fig. 15 NASA CC3 impeller passage. Instantaneous isosurfaces of Q , zoom on the suction side of the main blade.

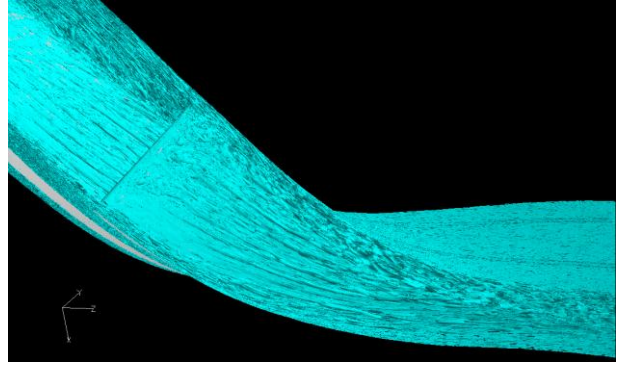


Fig. 16 NASA CC3 impeller passage. Instantaneous isosurfaces of Q , zoom on the suction side of the splitter blade

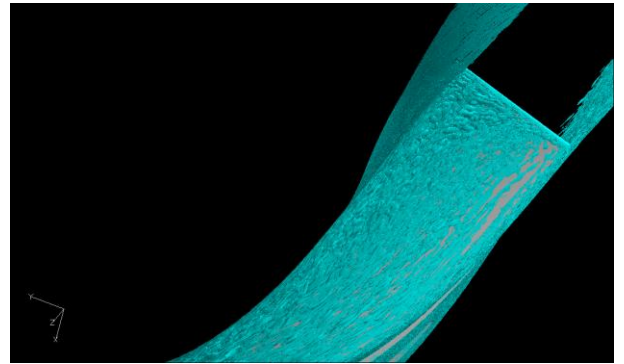


Fig. 17 NASA CC3 impeller passage. Instantaneous isosurfaces of Q , zoom on the pressure side of the main blade

Fig. 18 presents instantaneous axial velocity in the inlet region and in the vicinity of the leading edge of the blades. Results obtained using RANS with k - ω model on the initial grid, coarse LES and finer grid LES are compared side-by-side. Obviously, with increased resolution more flow structures emerge. An important thing to repeat is that all the LES computations conducted so far have been without turbulent fluctuations at the inlet which clearly has a big impact on the development of boundary layers on the hub and the shroud (as seen at the top of Fig. 18). A procedure to include the inlet fluctuations, following the approach in [19] is currently being implemented and will be tested next to assess its impact on the overall predictions.

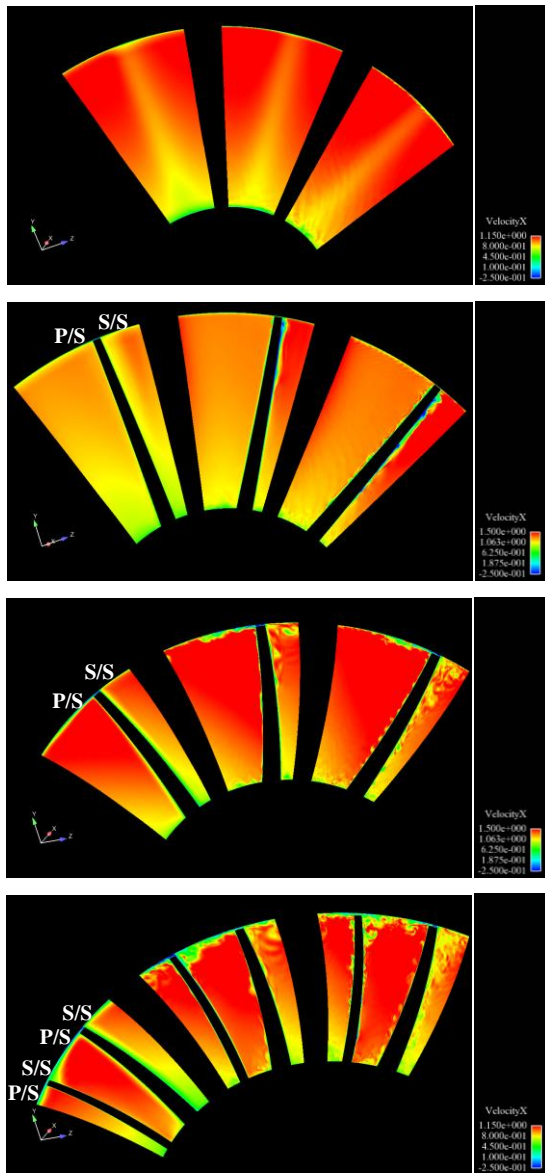


Fig. 18 NASA CC3 impeller passage. Instantaneous axial velocity at various axial cross-sections ($x = -0.25, 0.25, 1.75$ and 2.75 in); RANS on a grid with 1.2 million cells (left), LES with WALE sub-grid scale model on a grid with 9 million cells (middle), and a grid with 81 million cells (right).

Similarly, Fig. 19 presents the contours of instantaneous radial velocity towards the trailing edge of the blades. There are significant differences in the prediction of clearance flow, as well as the overall secondary flow pattern. More detailed comparisons with time-averages from LES analyses will allow for closer inspection of these differences.

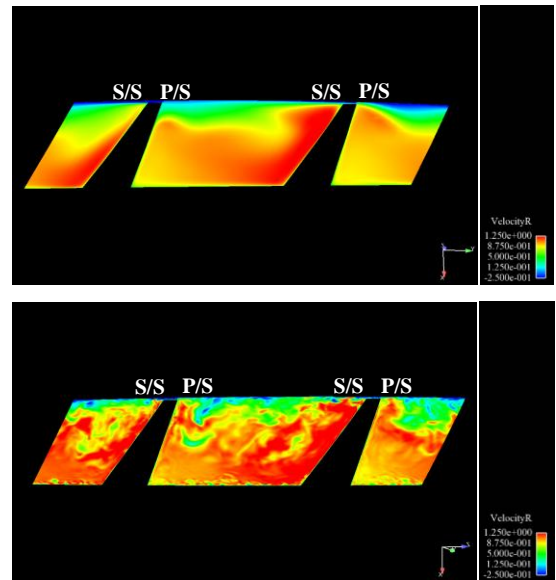


Fig. 19 NASA CC3 impeller passage. Instantaneous radial velocity at radial cross-sections $R = 7.5$ in (close to the trailing edge); RANS with 1.2 million cells (top), LES with WALE sub-grid scale model with 81 million cells (right).

CONCLUSIONS

Flow in a centrifugal impeller as well as several canonical test problems (rotating channel, straight and curved square duct) have been analyzed using the LES framework with WALE subgrid scale model. Detailed comparisons were made to results obtained with two-equation RANS turbulence models, hybrid RANS/LES approaches (k - ω based DES and SAS frameworks), and data (from DNS simulations and experiments). It has been shown that with increased grid resolution LES becomes capable of capturing the details of complex turbulent flow physics present in these cases. Special attention needs to be made to dissipative numerical discretization errors, suitable inlet boundary conditions, and as already mentioned, grid resolution.

ACKNOWLEDGMENTS

The authors would like to thank Drs. Ying Shi and Xiangyang Deng of UTRC-China for their contribution in setting up the canonical test cases at the beginning of this project.

REFERENCES

- [1]. VKI Lecture Series 2009-08, "Numerical investigations in turbomachinery: the state of the art", Edited by T. Arts and M. Manna, Von Karman Institute for Fluid Dynamics, Belgium.

- [2]. VKI Lecture Series 2010-08, "Effect of system rotation on turbulence with application to turbomachinery", Edited by M. Bilka and P. Rambaud, Von Karman Institute for Fluid Dynamics, Belgium.
- [3]. Nicoud, F. and Ducros, F., 1999, "Subgrid-scale stress modeling based on the square of the velocity gradient tensor", *Flow, Turbulence and Combustion*, Vol. 62, pp. 183-200.
- [4]. Strelets, M., 2001, "Detached eddy simulation of massively separated flows", AIAA Paper 2001-0879.
- [5]. Spalart, P. R., Jou, W. H., Strelets, M. and Allmaras, S. R., 1997, "Comments on the feasibility of LES of wings, and on a hybrid RANS/LES approach", 1st AFOSR Int. Conf. on DNS/LES, Aug. 4-8, 1997, Ruston, LA. In: *Advances in DNS/LES*, C. Liu and Z. Liu Eds., Greyden Press, Columbus, OH, USA.
- [6]. Menter, F. R., 1992, "Two-equation eddy-viscosity turbulence models for engineering applications", *AIAA Journal*, Vol. 32, pp. 1598-1605.
- [7]. Menter, F. R., 1993, "Zonal two-equation $k-\omega$ turbulence model for aerodynamic flows", AIAA Paper 1993-2906.
- [8]. Ni, R.-H., 1982, "A multiple-grid scheme for solving the Euler equations", *AIAA Journal*, Vol. 20(11), pp. 1565-1571.
- [9]. ANSYS CFX 12.0 User's Guide. ANSYS Inc. 2010.
- [10]. Comte-Bellot, G. and Corrsin, S., 1971, "Simple Eulerian time correlation of full- and narrow-band velocity signals in grid-generated, 'isotropic' turbulence", *Journal of Fluid Mechanics*, Vol. 48(2), pp. 273-337.
- [11]. Rogallo, R. S., 1981, "Numerical experiment in homogeneous turbulence", NSAS, TM81315.
- [12]. Moser R., Kim J. & Mansour, N., 1999, "DNS of Turbulent Channel Flow up to $Re_\tau = 590$ ", *Physics of Fluids*, Vol 11, pp. 943-945.
- [13]. Kim, J., Moin, P. and Moser, R., 1987. "Turbulence statistics in fully developed channel flow at low Reynolds number", *Journal of Fluid Mechanics*, Vol. 177, pp. 133-166.
- [14]. Kristoffersen, R. and Anderson H. I., 1993, "Direct simulation of low-Reynolds-number turbulent flow in a rotating channel", *Journal of Fluid Mechanics*, Vol. 256, pp. 163-197.
- [15]. Gavrilakis, S., 1992, "Numerical simulation of low Reynolds number turbulent flow through a straight square duct", *Journal of Fluid Mechanics*, Vol. 244, pp. 101-112.
- [16]. Humphrey, J. A. C., Taylor, A. M. K. and Whitelaw, J. H., 1977, "Laminar flow in a square duct of strong curvature", *Journal of Fluid Mechanics*, Vol. 83, pp. 509-527.
- [17]. Humphrey, J. A. C., Whitelaw, J. H. and Yee, G., 1981, "Turbulent flow in a square duct of strong curvature", *Journal of Fluid Mechanics*, Vol. 103, pp. 443-463.
- [18]. Sandham, N. D., Yao, Y. F. and Lawal, A. A., 2003. "Large-eddy simulation of transonic turbulent flow over a bump", *International Journal of Heat and Fluid Flow*, Vol. 24, pp. 584-595.
- [19]. Lund, T.S., Wu, X., and Squires, K.D., 1998, "Generation of turbulent inflow data for spatially developing boundary layer simulation", *Journal of Computational Physics*, Vol. 140, pp. 233-258.
- [20]. Skoch, G. J, Prahst, P. S, Wernet, M., Wood, J. and Strazisar, A., 1997, "Laser anemometer measurements of the flow field in a 4:1 pressure ratio centrifugal impeller", ASME Paper 97-GT-342.